Nucleic Acids Research, 2025, **53**, gkaf099
https://doi.org/10.1093/nar/gkaf099
Nucleic Acid Enzymes

Mitochondrial exonuclease EXOG supports DNA integrity by the removal of single-stranded DNA flaps

Anna Karlowicz [1], Andrzej B. Dubiel [1], Marta Wyszkowska [1], Kazi Amirul Hossain [2], Jacek Czub [2], Michal R. Szymanski [1,*]

[1]Structural Biology Laboratory, Intercollegiate Faculty of Biotechnology of University of Gdansk and Medical University of Gdansk, University of Gdansk, Abrahama 58, 80-307 Gdansk, Poland
[2]Department of Physical Chemistry, Gdansk University of Technology, ul. Narutowicza 11/12, 80-233 Gdansk, Poland
[*]To whom correspondence should be addressed. Email: michal.szymanski@ug.edu.pl

Abstract

Single-stranded DNA (ssDNA) is an important intermediate generated during various cellular DNA transactions, primarily during long-patch base excision repair. When displaced by DNA polymerase during strand displacement DNA synthesis, ssDNA forms 5′ overhangs (flaps) that are either cleaved by DNA nucleases or protected from degradation upon binding of single-stranded DNA-binding proteins (SSB). Several nucleases are involved in the removal of ssDNA flaps in human mitochondria, namely the endonucleases FEN1 and DNA2, as well as the exonuclease MGME1. In this study, we show that another mitochondrial nuclease, EXOG, cleaves DNA flaps in both free and SSB-protected forms. We established that the presence of the Wing domain in EXOG structure provides additional binding site for ssDNA and 5′ flaps irrespective of monovalent salt concentration. Importantly, DNA flap cleavage by EXOG is compatible with the activity of other mitochondrial enzymes involved in DNA replication/repair, e.g. mtSSB, Pol γ, and Lig III, as we were able to reconstitute a multistep reaction of DNA synthesis, flap removal, and nick ligation. Our findings highlight the versatile role of EXOG in maintaining mitochondrial DNA integrity, expanding its DNA processing repertoire to include ssDNA flap removal.

Graphical abstract

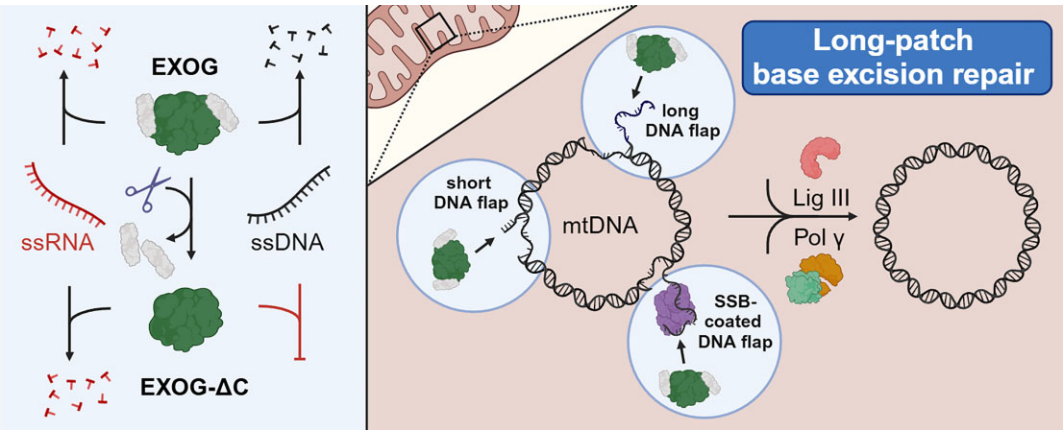

Introduction

Genomes of mitochondria (mtDNA) are distinct from nuclear genomes and structurally similar to prokaryotic DNA, which is explained by the bacterial origin of mitochondria (reviewed in [1]). In humans, mtDNA is a double-stranded circular molecule of merely 16.6 kbp (compared to 3.2 Gbp of the haploid nuclear genome). Nevertheless, due to its presence in multiple copies per cell, mtDNA constitutes a significant fraction of total cellular DNA [2]. It encodes 13 proteins that constitute critical core components involved in cellular respiration, thus making mtDNA essential to life. Importantly, human mtDNA consists of densely packed exons (over 90% of the sequence), with no introns, and only one major non-coding region that controls its replication and transcription. Therefore, every mutation in mtDNA can be detrimental to the function of mitochondria. Considering that the mitochondrial environment is highly genotoxic due to the close proximity of the electron transport chain and elevated levels of

Received: February 27, 2024. **Revised:** January 27, 2025. **Editorial Decision:** January 29, 2025. **Accepted:** February 4, 2025

reactive oxygen species (ROS), the maintenance of mtDNA integrity and stability is crucial to mitochondrial functions and thus the health of our cells. As loss of mtDNA integrity is related to both early-onset and age-related diseases [3], our understanding of factors affecting mitochondrial genome stability is clinically relevant for the development of useful biomarkers and therapeutic strategies.

Cells employ DNA repair mechanisms to cope with DNA damage. While several DNA repair pathways have been proposed to take place in mitochondria [4–6], base excision repair (BER) is considered the predominant pathway. BER is largely responsible for removing nonbulky DNA lesions resulting from oxidation, deamination, or alkylation [7]. These lesions do not distort the DNA structure but may lead to DNA replication errors or hinder DNA replication enzymes. The general steps of the BER pathway include excision of the damaged base, cleavage of the DNA backbone at the abasic site, DNA end processing, gap filling, and ligation. When gap filling requires a single nucleotide insertion, followed by ligation of the intact DNA ends, short-patch BER (SP-BER) is sufficient. It may happen, however, that either 3′ or 5′ end (or both) of a strand break is modified, which corrupts a continuous strand generation, leading to defective replication and contributing to the formation of highly genotoxic double-stranded DNA breaks [8]. Modifications at the 5′ end originate from either further chemical alterations (e.g. secondary ROS insult) or protein–DNA adducts formation [9], whose repair requires more than one nucleotide replacement via an alternative long-patch BER (LP-BER) subpathway. Evidence on the existence of LP-BER *in vivo* was reported for mammalian cells [10] as well as mitochondrial extracts [9, 11, 12].

The mechanism of LP-BER assumes strand displacement DNA synthesis performed by replicative DNA polymerases at the modified lesion site, which results in the generation of single-stranded 5′ overhangs (flaps) [13, 14]. These overhangs need to be processed by dedicated nucleases to generate the appropriate substrate for DNA ligation. Long single-stranded DNA (ssDNA) fragments generated in a cell are protected by single-stranded DNA-binding (SSB) proteins from immediate degradation. SSB proteins bind ssDNA tightly with no sequence specificity, which facilitates DNA organization as well as recruitment of other proteins to their sites of action [15, 16]. Mitochondria contain their own SSB (mtSSB), which forms a stable tetramer [17] similar to SSB from *Escherichia coli* [18]. mtSSB is an essential component of the mitochondrial DNA replication machinery [19]; not only does mtSSB protect ssDNA at the replication fork and support other replication proteins [20–22] but also restricts primer formation to origins of replication and stabilizes R-loop formation, which is important to balance replication and transcription of mtDNA [23].

DNA nucleases (DNases) play a vital role in DNA maintenance. In mitochondria, several nucleases are implicated in ssDNA processing: mitochondrial genome maintenance exonuclease 1 (MGME1) [24], flap endonuclease 1 (FEN1) [9], DNA replication ATP-dependent helicase/nuclease (DNA2) [25], and endo/exonuclease G (EXOG) [26]. MGME1 is exclusively localized to mitochondria, and its role as a flap nuclease in mtDNA maintenance was evidenced by several studies, including the examination of MGME1 mutations reported in patients [24, 27–29]. FEN1 and DNA2 are well-known flap endonucleases essential during Okazaki fragments maturation in nuclear DNA replication [30–34]. The role of FEN1 in maintaining mtDNA integrity [35] and BER [9] was reported; however, its mitochondrial localization and activity was shown to be dependent on the cell type tested [9, 11, 12, 25, 35–37]. DNA2 was demonstrated to be important in LP-BER in mitochondria as well as RNA primer processing during mtDNA replication [25, 38, 39]. Finally, EXOG, a 5′ exo/endonuclease found in mitochondria of higher eukaryotes [40], was shown to contribute to the processing of single-strand breaks containing 5′-blocking oxidized deoxyribose as well as to provide critical nuclease activity for LP-BER in mitochondrial extracts [11, 26]. Due to the diversity of mitochondrial nucleases and putative cell-type specificity, the exact mechanism of DNA end-processing step during LP-BER in mitochondria is not clear.

Here, we examined human nuclease EXOG for its ability to process DNA flaps. EXOG localizes exclusively to mitochondria [40] and was shown to be involved in mtDNA repair and maintenance of mitochondrial function [26, 41, 42]. Structural and biochemical studies revealed that EXOG is a sugar-nonspecific nuclease that cleaves a variety of substrates, including ssDNA, double-stranded DNA (dsDNA), and abasic sites (BER intermediates) [40, 43, 44] as well as RNA in RNA flaps and RNA/DNA duplexes [37, 45] supporting its role in RNA primer removal in mitochondria. EXOG is a paralog of an unspecific endonuclease EndoG [46] and both belong to a ββα-Me nuclease family [47]. Both enzymes are homodimers with nearly identical Core domains [43, 48]. Notably, EXOG possesses a distinctive C-terminal Wing domain, which has been demonstrated to confer substrate specificity critical for mtDNA repair [43]. Here, we show that the Wing domain of EXOG also contributes to the binding and precise positioning for cleavage of ssDNA but not ssRNA. Moreover, we found that EXOG cleaves ssDNA flaps of various lengths and efficiently removes long, mtSSB-coated DNA flaps. Finally, by reconstituting a ligation reaction preceded by DNA synthesis and DNA flaps cleavage in the presence of mitochondrial polymerase Pol γ, mtSSB, and DNA ligase Lig III, we demonstrate that EXOG supports the activity of other mitochondrial enzymes critical for the maintenance of mtDNA.

Materials and methods

Protein purification

All proteins were purified as previously described: EXOG, EXOG-ΔC68, and EXOG-R109A (all EXOG variants are His-tagged recombinant human proteins lacking mitochondrial targeting sequence (MTS) and *trans*-membrane domain, ΔN58) [43], nontagged human mtSSB (amino acids 18–148) [37], His-tagged recombinant Pol γA (lacking MTS and 10 of the 13 sequential glutamine residues 43–52) [49], His-tagged recombinant Pol γB (lacking MTS) [49], and His-SUMO-tagged human Lig IIIα protein (lacking MTS) [50]. Throughout this manuscript, "EXOG" is used to refer to the truncated variant EXOG-ΔN58. The concentrations of the protein preparations were determined spectrophotometrically using the following extinction coefficients ϵ_{280}: 77 030 M^{-1} cm^{-1} (EXOG and EXOG-R109A dimers), 68 090 M^{-1} cm^{-1} (EXOG-ΔC68 dimer), 79 760 M^{-1} cm^{-1} (mtSSB tetramer), 242 295 M^{-1} cm^{-1} (Pol γA monomer), 143 280 M^{-1} cm^{-1} (Pol γB dimer), and 79 988 M^{-1} cm^{-1} (Lig IIIα monomer).

Thermal unfolding

Thermal stability of EXOG and EXOG-ΔC68 was measured using Tycho (NanoTemper). It is capillary-based technique that detects changes in the intrinsic fluorescence of proteins upon thermal unfolding. Changes in fluorescence signal detected at 350 and 330 nm (from tryptophan and tyrosine residues) in temperature gradient indicate the transition from folded to unfolded state of a protein, reflected as the inflection temperature (T_i). Proteins were analyzed at a concentration of 0.3 μg/μl.

Preparation of DNA substrates

Oligonucleotides used in this study (Supplementary Table S1) were purchased from Metabion International AG. All the linear duplex substrates (S1–S20 and Supplementary Table S2) were formed with a downstream 3′-fluorescein-labeled oligonucleotide (D), an upstream oligonucleotide (U) with a bottom template (B) and mixed at D:U:B = 1.0:1.1:1.1 molar ratio. The circular substrates (S21 and S22, and Supplementary Table S2) were formed with a primer oligonucleotide and a circular template at 1:1 molar ratio. ssDNA ligase (CircLigase II, Epicentre) was used to obtain a circular template. The annealing of substrates was performed by incubation at 95°C for 5 min in 20 mM Tris–HCl, pH 8.1, 0.1 mM EDTA, and slowly cooled to room temperature.

Exonuclease activity assay

Reaction conditions are detailed in the figure captions. All assays were performed in a buffer containing 20 mM HEPES, pH 7.5, 140 mM KCl (unless stated otherwise), 1 mM tris(2-carboxyethyl)phosphine (TCEP), and 0.1 mg/ml bovine serum albumin (BSA). Reactions were initiated by the addition of an equal volume of substrates (listed in Supplementary Tables S1 and S2) and incubated at room temperature for indicated time periods. Reactions were stopped with 78% formamide, 50 mM EDTA, and 0.1% SDS, followed by incubation at 95°C for 4 min. Samples were resolved by denaturing urea–PAGE and visualized using Typhoon scanner platform [RGB (Cytiva) or Variable Mode Imager (Amersham Biosciences)]. Quantification of the data was performed using ImageJ (https://imagej.net/ij/index.html) [51].

Steady-state kinetics

Steady-state kinetic reactions were performed in a buffer containing 20 mM HEPES, pH 7.5, 140 mM KCl, 1 mM TCEP, and 0.1 mg/ml BSA under varying concentrations of ssDNA (O1 and Supplementary Table S1) or ssRNA (O2 and Supplementary Table S1) substrate (25, 50, 100, and 200 nM) and the constant concentration of EXOG (2.5 nM). Reaction mixtures were pre-equilibrated on ice for 5 min and then equilibrated at 25°C for 2 min. Reactions were initiated with 10 mM $MgCl_2$ and incubated at 25°C. At indicated time points (0, 0.25, 0.5, 0.75, 1, 1.25, 1.5, 2, 2.5, and 3 min) aliquots of the reaction were removed and stopped with 78% formamide, 50 mM EDTA, and 0.1% SDS, followed by incubation at 95°C for 4 min. Samples were resolved by denaturing urea–PAGE and visualized using Typhoon scanner platform [RGB (Cytiva) or Variable Mode Imager (Amersham Biosciences)]. Quantification of the data was performed using ImageJ (https://imagej.net/ij/index.html) [51]. The sum of cleavage products was used for quantifications. Polynomial trendline with non-zero intercept was used to plot the concentration of product as a function of time to obtain initial velocities of the enzyme. The resulting velocities as a function of substrate concentration were fit to the Michaelis–Menten equation (Polymath^{Plus} Solver) to obtain V_{max} and K_m. k_{cat} was calculated from V_{max}/[EXOG].

Ligation assay—linear substrates

Reaction mixtures contained 200 nM substrate, 5 nM EXOG, 150 nM Pol γA, 600 nM Pol γB, and 200 nM Lig III in 20 mM HEPES, pH 7.5, 140 mM KCl, 1 mM TCEP, and 0.1 mg/ml BSA supplemented with 10 mM $MgCl_2$, 1 mM ATP, 1 mM deoxynucleoside triphosphates (dNTPs), and 1.89 μM streptavidin (New England BioLabs). After 10-min incubation at 37°C, unlabeled competitor DNA oligonucleotide C1 (Supplementary Table S1) was added to the final concentration of 10 μM, followed by further incubation at 37°C for 1 h. Reactions were stopped with 78% formamide, 50 mM EDTA, 0.1% SDS, incubated at 95°C for 4 min and resolved by denaturing urea–PAGE. Gels were imaged with Typhoon scanner platform [RGB (Cytiva) or Variable Mode Imager (Amersham Biosciences)]. Substrate and product bands were quantified using ImageJ (https://imagej.net/ij/index.html) [51].

Ligation assay—circular substrates

Reaction mixtures containing 2.5 nM substrate, 12.5 nM Pol γA, 25 nM Pol γB, and 2.5 nM mtSSB in 20 mM HEPES, pH 7.5, 140 mM KCl, 1 mM TCEP, and 0.1 mg/ml BSA supplemented with 10 mM $MgCl_2$, 1 mM ATP, 0.5 μM unlabeled dNTPs, and 2.5 nM [α-^{32}P] deoxycytidine triphosphate (dCTP; 800 Ci/mmol, 10 mCi/ml; Hartmann Analytic) were preincubated for 20 min at 37°C, followed by the addition of 750 pM EXOG and 25 nM Lig III, and further incubation at 37°C for 1 h. The reactions were stopped by the addition of Proteinase K (A&A Biotechnology) to the final concentration of 200 μg/ml and incubated at 48°C for 1 h. Reactions were stopped with 78% formamide, 50 mM EDTA, 0.1% SDS, incubated at 65°C for 2 min and resolved by denaturing urea–PAGE. Gels were dried and visualized using Typhoon scanner platform [RGB (Cytiva) or Variable Mode Imager (Amersham Biosciences)].

Microscale thermophoresis

The binding affinity of EXOG and EXOG-ΔC68 for ssDNA and ssRNA was measured using the microscale thermophoresis (MST) with Monolith NT.115 (NanoTemper) at 25°C. ssDNA/ssRNA 16-mer labeled at 3′ end with Cy5 (O10 and O11, Supplementary Table S1) at a final concentration of 5 nM was used as a target. The increasing concentrations of EXOG (300 pM to 10 μM) and EXOG-ΔC68 (50 pM to 2 μM) were used as ligands. Measurements were carried out in 20 mM HEPES, pH 7.5, 140 mM KCl, 1 mM TCEP, and 0.009% NP-40. In MST analysis, a ligand-dependent change in the initial fluorescence was observed. The apparent dissociation constant ($K_{d,app}$) was determined using a single-site model with MO Affinity Analysis software version 2.3 [52, 53].

Molecular dynamics simulations

To model the structures of EXOG bound to both ssDNA and ssRNA, we utilized the crystal structure available in the Pro-

tein Data Bank (PDB ID: 5T5C; [43]). The complementary DNA strand was removed, the length of both ssDNA and ssRNA were limited to 5 nucleotides with the following sequence: 5′-CGCAC-3′. The EXOG-ΔC68 and EXOG-R109A mutants were generated by deleting the Wing domain and mutating R109 to alanine, respectively.

Molecular dynamics (MD) simulations were conducted using Gromacs 2023 [54] and the Amber-parmbsc1 force field [55] within the isothermal–isobaric (NPT) ensemble. Temperature was maintained at 300 K using the v-rescale thermostat [56] with a time constant of 0.1 ps, and the pressure was controlled at 1 bar with the isotropic Parrinello–Rahman barostat [57]. Periodic boundary conditions were applied in three dimensions, and long-range electrostatic interactions were computed using the particle mesh Ewald (PME) method [58] with a real-space cutoff of 1.2 nm and a Fourier grid spacing of 0.12 nm. Van der Waals interactions were modeled using the Lennard–Jones potential with a cut-off of 1.2 nm and a switching distance of 1 nm. For protein and DNA, bond lengths were constrained using P-LINCS [59], while water molecule geometry was constrained with SETTLE [60]. Integration of the equations of motion was performed using the leap-frog algorithm with a time step of 2 fs. Each simulation was run for a duration of 1–1.5 μs and initial 20%–30% of the trajectories were discarded as equilibration. In total, approximately ∼15 μs of sampling time was achieved.

Per-residue contributions to the overall EXOG-substrate binding energy (E) were computed by summing the electrostatic and van der Waals interaction energies between the Core domain residues of EXOG (located within 5 Å of the first 3 nucleotides of either ssDNA or ssRNA) and the respective oligonucleotide substrates. To assess how these contributions change following the deletion of the Wing domain, we subtracted the values obtained for the EXOG from those obtained for the EXOG-ΔC68 mutant. Positive changes in interaction energy (ΔE) denote residues whose contribution to complex stability weakens after the deletion, while negative changes indicate the stability enhancement.

Hydrogen bonds (Hb) were identified between the same EXOG residues and the oligonucleotide backbone using the GROMACS hbond module from the MD trajectories. Standard geometrical criteria were used for defining Hb, with cutoffs of 0.35 nm for the donor–acceptor distance and 30° for the hydrogen donor–acceptor angle.

Results

The Wing domain in EXOG structure is essential for binding single-stranded DNA but not RNA

We have previously shown that the C-terminal Wing domain of EXOG provides substrate specificity [43] and distinguishes EXOG from its nonspecific paralog, EndoG (Fig. 1A and B). Here, we compared the nuclease activity of EXOG and the Wing domain deletion mutant, EXOG-ΔC68, on a 20-mer ssDNA heterooligonucleotide (O1 and Supplementary Table S1). Already at 2.5 nM concentration of EXOG, ∼70% of ssDNA (400 nM) was processed after 5 min (Fig. 1C and lane 3). Interestingly, we did not observe the cleavage of ssDNA by EXOG-ΔC68 (Fig. 1C and lanes 6–8); even at increased concentrations of the mutant its activity was negligible (Fig. 1C and lanes 9–12). Importantly, EXOG-ΔC68 has previously been demonstrated to be active on dsDNA [43]. The lack of activity of EXOG-ΔC68 on ssDNA substrate prompted us to examine the interaction between EXOG variants and ssDNA. Using the MST, we did not detect the binding of EXOG-ΔC68 to 3′ Cy5-labeled ssDNA, while EXOG formed a complex with the ssDNA substrate with an apparent dissociation constant ($K_{d,app}$) of 25.1 ± 4.5 nM (Fig. 1F and Supplementary Fig. S1A). The protein quality test revealed nearly identical unfolding temperatures for both EXOG variants (Supplementary Fig. S2); therefore, we hypothesized that the disruption of ssDNA-EXOG-ΔC68 complex formation could stem from the lack of the Wing domain in the EXOG-ΔC68 structure. Our reactions were conducted at 140 mM KCl concentration, resembling physiological ionic strength within the mitochondria [61]. As electrostatic interactions are reduced at higher salt, we decreased the KCl concentration to 10 mM in our cleavage reactions and, indeed, the processing of ssDNA by the EXOG-ΔC68 variant was observed, although not at the level of EXOG (Fig. 1C, and lanes 13–23 and 1E).

In recent reports, both our group and others showed that, besides DNA, EXOG processes ssRNA [37, 45]. To compare the efficiency of cleavage between ssDNA and ssRNA, we examined the cleavage activity of the EXOG variants on ssRNA (O2 and Supplementary Table S1) that corresponds in sequence and length with the ssDNA tested above. We found that, in contrast to ssDNA, ssRNA is cleaved more efficiently by the ΔC68 mutant at 140 mM KCl when compared with EXOG (Fig. 1D and lanes 2–8). Interestingly, the cleavage of ssRNA at 10 mM KCl remained mostly unaffected for both variants (Fig. 1D and E, and lanes 9–15). Analysis of MST binding data revealed $K_{d,app}$ of 6.2 ± 1.8 nM for ssRNA–EXOG, which indicates a slightly stronger affinity of EXOG to ssRNA compared with ssDNA (Fig. 1F and Supplementary Fig. S1B). Stronger binding of the substrate in the active site might contribute to a slower dissociation rate after cleavage. It might explain our observations that EXOG cleaves ssDNA more efficiently than ssRNA, as <2.5 nM concentration of EXOG is required to cleave 50% of ssDNA while >15 nM is needed to cleave 50% of ssRNA under the same reaction conditions (Supplementary Fig. S3). The EXOG-ΔC68 variant exhibits significantly lower affinity for ssRNA compared with EXOG ($K_{d,app}$ = 155 ± 31.9 nM; Fig. 1F and Supplementary Fig. S1B). Together, our results indicate that the Wing domain is responsible for conferring the ssDNA substrate specificity on EXOG.

The Wing domain and R109 residue of the Core domain are essential for stable positioning of ssDNA in the active site of EXOG

To gain structural insights into the role of the Wing domain in the single-stranded substrate specificity of EXOG, we conducted MD simulations. Specifically, we investigated the dynamical behavior of both ssDNA and ssRNA (5-mers) bound to EXOG as well as the EXOG-ΔC68 variant. Our previously published structure of the dsDNA–EXOG complex [43] revealed the importance of the Wing domain in a precise positioning of the phosphodiester backbone of the substrate strand within the catalytic region of the enzyme, thus facilitating an incision between the second and third nucleotides (scissile bond). Assuming the same first scissile bond for ssDNA and ssRNA substrates, we compared the center-of-mass (COM) distance between the amino acid residues in the catalytic site of the EXOG variants and the scissile phosphate

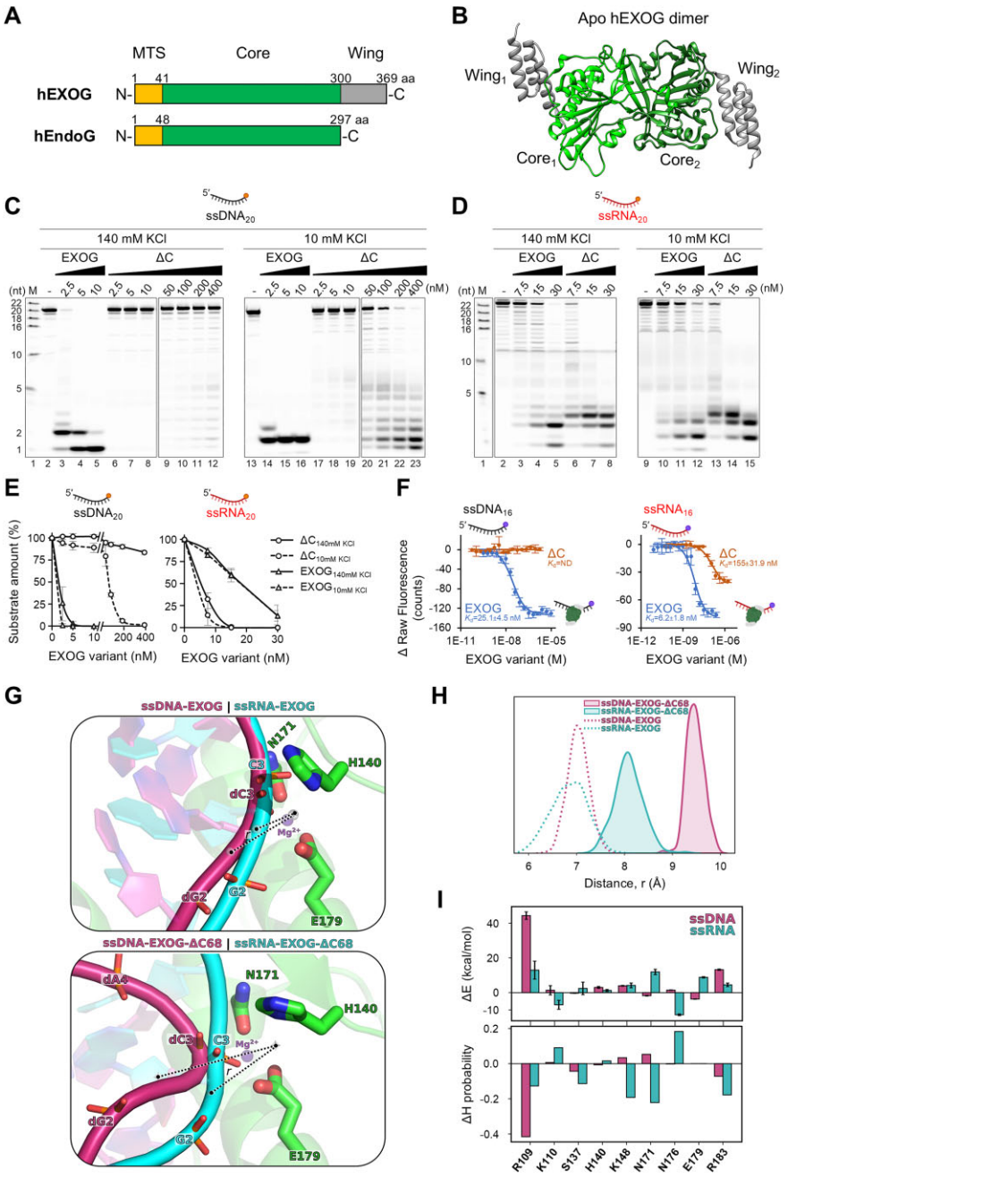

Figure 1. Cleavage of ssDNA by EXOG requires the presence of the Wing domain. (**A**) Scheme of the domain composition of human EXOG and human EndoG. Numbers indicate amino acid positions; MTS, mitochondrial targeting sequence. Structure was rendered in UCSF ChimeraX [79] (**B**) Structure of apo hEXOG-ΔN58 dimer (PDB: 5T40 [43]) lacking MTS, *trans*-membrane domain, and a predicted unstructured region. (**C**) 400 nM of ssDNA (O1 and Supplementary Table S1) was incubated with the increasing concentration of EXOG or EXOG-ΔC68 (nM) in the presence of 10 mM $MgCl_2$. Reaction buffer contained either 140 mM or 10 mM KCl. After 5 min of incubation at RT, reactions were stopped and analyzed using urea–PAGE. *M*, molecular-weight size marker. (**D**) Reactions as in (C), except that ssRNA (O2 and Supplementary Table S1) was used as a substrate. (**E**) Densitometric analysis of the substrates in panels (C) and (D). The graphs represent the mean values with standard deviations (error bars) from three experiments. (**F**) Change of fluorescence signal related to the titration of EXOG and EXOG-ΔC68 against Cy5-labeled ssDNA (left, O10 and Supplementary Table S1) or ssRNA (right, O11 and Supplementary Table S1) as a target. Fit of the changes in the fluorescence signal to a single-site binding model yielded a $K_{d,app}$ of 25.1 ± 4.5 nM for EXOG-ssDNA, 6.2 ± 1.8 nM for EXOG-ssRNA and 155 ± 31.9 nM for EXOG-ΔC68-ssRNA. No binding was detected for EXOG-ΔC68-ssDNA (ND, not detected). Error bars indicate the standard deviation in a triplicate of experiments. Raw MST traces are provided in Supplementary Fig. S1A and B. (**G**) The active site of representative models of EXOG (top) and EXOG-ΔC68 (bottom) in a complex with ssDNA (magenta) and ssRNA (cyan) oligonucleotides (5-mers). Residues in the catalytic region (H140, N171, and E179) and phosphate groups of the substrate backbones are shown in stick representation, with their corresponding COM shown as transparent white spheres with the measured distance (*r*) shown in dashed black lines. The magnesium ion is represented as a purple sphere. (**H**) Distribution of COM distances (*r*) between residues in the catalytic region and phosphate groups, calculated from MD trajectories. Dotted and solid lines correspond to EXOG and EXOG-ΔC68, respectively. (**I**) Top: Change in the per-residue contributions to the overall substrate binding energy (Δ*E*) following the deletion of the Wing domain. The Core domain residues located within 5 Å of the first three nucleotides of ssDNA or ssRNA were analyzed (see Supplementary Fig. S4A). Bottom: Change in Hb probability for the same Core domain residues following the deletion of the Wing domain. The bars represent subtracted values obtained for EXOG from those obtained for EXOG-ΔC68 (Supplementary Fig. S4B).

group of each single-stranded substrate (Fig. 1G). The average distance between the catalytic site of EXOG and both substrates is very similar (∼7 Å; Fig. 1H, dotted lines), with ssRNA exhibiting a marginally tighter binding. Conversely, we observed a pronounced increase (>2.5 Å) in the COM distance between ssDNA and the active site of EXOG-ΔC68 (Fig. 1H, solid magenta line), indicating a significant displacement of ssDNA from the catalytic region (Fig. 1G and Supplementary Fig. S4A); ssRNA, on the contrary, remains firmly bound to the Core domain upon the Wing domain deletion, with a modest increase in the COM distance (∼1 Å; Fig. 1H, solid cyan line).

To investigate in more detail the observed differences in positioning of each single-stranded substrate in the active site of EXOG-ΔC68, we further analyzed how the individual per-residue contributions to the overall binding energy of the substrate–EXOG complexes change upon the deletion of the Wing domain. The binding energy changes (ΔE) were calculated for all the residues of the Core domain of EXOG located within 5 Å from the first three nucleotides (from 5′ end) of either ssDNA or ssRNA (Supplementary Fig. S4A). A positive (unfavorable) value of ΔE indicate that the contribution of a residue to the complex stability decreases upon the Wing domain deletion, thus weakening the complex interaction; a negative (favorable) value of ΔE indicates a stronger interaction. The obtained data show that the Wing domain deletion leads to a distinct weakening of the ssDNA–EXOG interaction, as indicated by positive ΔE values (Fig. 1I, top panel, magenta bars), particularly affecting the contribution of R109 and, to a lesser extent, R183. By contrast, the weakening of the interactions between the Core domain residues and ssRNA is significantly less pronounced, including the increased contribution to the complex stability of N176 and K110 (Fig. 1I, top panel, cyan bars).

In addition to the binding energy changes, we examined changes in Hb formation probability between the same residues of the Core domain of EXOG and the backbone of both oligonucleotide substrates following the Wing domain removal. The changes in Hb formation probability largely correlate with ΔE (Fig. 1I, bottom panel, and Supplementary Fig. S4B). Regarding ssDNA binding, R109 is mostly affected by the Wing domain deletion, having significantly decreased probability of Hb formation (magenta bars). For the ssRNA–EXOG interaction after the Wing domain removal, we observed both decreased and increased probability of Hb formation, depending on the residue in the active region (Fig. 1I, cyan bars). More detailed examination revealed that the additional hydrogen bonding interactions can be partially attributed to the presence of the 2′-OH group on the pentose ring of the RNA ribose (Supplementary Fig. S4B, bottom panel, light cyan bars).

As arginine R109 emerged to be significantly affected by the Wing domain deletion in our *in silico* analyses of ΔE and Hb formation probability regarding ssDNA binding to EXOG, we additionally investigated the behavior of both substrates interacting with the EXOG-R109A mutant. To this end, similarly to the EXOG-ΔC68 variant, we measured the COM distance between the scissile phosphate group of each oligonucleotide and the amino acid residues in the catalytic site of the EXOG-R109A variant. Remarkably, the distance distribution is very similar to EXOG-ΔC68, implying a partial displacement of ssDNA but not ssRNA upon the R109A mutation introduction (Supplementary Fig. S4C and Fig. 1H). To confirm our *in silico* findings, we constructed, purified, and examined the nuclease activity of the EXOG-R109A mutant. We obtained strikingly similar activity of EXOG-R109A to EXOG-ΔC68: we did not observe the cleavage of ssDNA, while ssRNA was cleaved more efficiently when compared with EXOG (Supplementary Fig. S4D and E). This finding indicates that R109 in the catalytic region of EXOG, similarly to the Wing domain, plays a significant role in ssDNA but not ssRNA processing.

In summary, our MD analysis indicate that the Wing domain in EXOG structure stabilizes the interaction of the ssDNA with the amino acid residues in the active region, which is crucial for the substrate to be precisely positioned in the active site for the cleavage. However, it is not the case for ssRNA substrate as the Wing domain deletion has a minor overall impact on ssRNA-binding stability, most likely due to different chemical nature of RNA from DNA. Interestingly, we detected R109 in the catalytic domain of EXOG to be equally important in ssDNA but not ssRNA stability in the active site, which is also reflected by the results of our *in vitro* nuclease activity examination.

Table 1. Initial velocities were obtained from time-course reactions with the increasing concentrations of substrates (25–200 nM) and the constant concentration of EXOG (2.5 nM)

Substrate	K_m (nM)	k_{cat} (min^{-1})	k_{cat}/K_m (nM^{-1} min^{-1})
ssDNA	727 ± 187	103 ± 35	0.14
ssRNA	643 ± 127	37 ± 1	0.06

To obtain V_{max} and K_m, the initial velocities were fit to the Michaelis–Menten equation as a function of substrate concentration. k_{cat} is calculated from V_{max}/[EXOG]. Errors represent SD ($n = 3$). Representative gel-based analysis in Supplementary Fig. S5.

Characteristics of single-stranded substrate cleavage by EXOG

To compare the catalytic efficiencies of EXOG with ssDNA and ssRNA, we performed steady-state kinetic analysis in time-course reactions under varying concentrations of substrates (25–200 nM) and the constant concentration of EXOG (2.5 nM). The resulting initial velocities as a function of substrate concentration were fit to the Michaelis–Menten equation to obtain k_{cat} and K_m values. In our kinetic assay, we were unable to obtain one-site cleavage products due to the nature of EXOG activity with single-stranded substrates. Therefore, we used the sum of products for our quantifications, as was previously published for MGME1 exonuclease [62]. The results are summarized in Table 1. For both substrates K_m values are comparable; however, >2-fold higher k_{cat} was obtained with ssDNA than ssRNA. This resulted in an ∼2-fold higher catalytic efficiency (k_{cat}/K_m) of ssDNA cleavage by EXOG relative to ssRNA. Therefore, the affinity of both substrates to the active site of EXOG is comparable, consistent with our MST binding results (Fig. 1F); however, the turnover of ssDNA at the active site of EXOG is much faster than ssRNA, resulting in more efficient cleavage reaction.

The unevenly distributed band pattern in the gel, visualized after the cleavage of ssDNA heterooligonucleotide, revealed certain cleavage site preferences of EXOG (Fig. 2A and lanes 2–6). Therefore, we examined the cleavage efficiency of EXOG on homooligonucleotides dT_{20}, dC_{20}, dA_{20}, and U_{20} in a time-course experiment. We were not able to test dG_{20} as it is prone to form higher-ordered structures [63], which

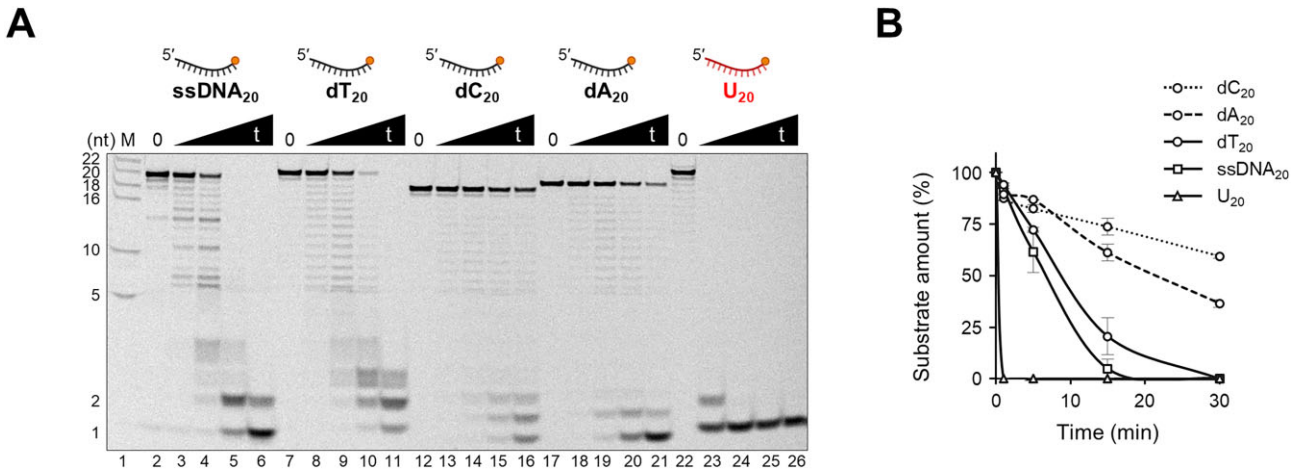

Figure 2. Homooligonucleotides are cleaved by EXOG with different efficiency. (**A**) 400 nM of each substrate (20-mer DNA heterooligonucleotide O1, dT_{20} O3, dC_{20} O4, dA_{20} O5, and U_{20} O6; Supplementary Table S1) was incubated with 1 nM EXOG in the presence of 10 mM $MgCl_2$. Reactions were stopped at indicated time points (0, 1, 5, 15, and 30 min) and analyzed using urea–PAGE; *M,* molecular-weight size marker. (**B**) Densitometric analysis of the substrates in panel (A). The graph represents the mean values with standard deviations (error bars) from two experiments.

are difficult to visualize, even in denaturing conditions. Unlike heterooligonucleotides, RNA homooligonucleotide U_{20} is the most effectively degraded among tested substrates (Fig. 2A and B, and lanes 22–26). The cleavage is very rapid even under the conditions of excess substrate (1 nM of EXOG and 400 nM of substrate). PolyU does not form any secondary structures at physiological temperatures [64] therefore poses no potential structural obstacles during binding to the active site of EXOG. The cleavage of dT_{20} was the most efficient among the DNA homooligonucleotides tested (Fig. 2A and B, and lanes 7–11), while the slowest degradation was observed for dC_{20} (Fig. 2A and B, and lanes 12–16). In each case, intermediate products of degradation are visualized as evenly distributed bands, except for the DNA heterooligonucleotide (Fig. 2A and lanes 2–6). This suggests that successive cleavage occurs in a processive manner. Given that natural sequences are typically nonuniform, the degradation of single-stranded substrates by EXOG might be processive, but the efficiency of each incision could be rate-limited by the type of consecutive nucleotide.

During the metabolism of mitochondrial DNA, ssDNA intermediates of different length may be formed; therefore, we also investigated whether the length of ssDNA substrate affects the cleavage efficiency by EXOG. To avoid sequence-dependent cleavage, we examined nucleolytic activity of EXOG using homooligonucleotides of different length. A 10-mer and longer dT oligonucleotides are cleaved with similar efficiency (Supplementary Fig. S6 and lanes 7–24). The shortest 5-nt long dT oligonucleotide is cleaved by EXOG with the lowest efficiency as <50% of the substrate was processed after 30 min (Supplementary Fig. S6 and lanes 1–6). These results correspond to our previously published data showing the efficiency of ssRNA cleavage of various lengths [37] and together indicate that EXOG is able to cleave efficiently single-stranded DNA or RNA >5 nucleotides.

Divalent metals, such as Ca^{2+}, Mg^{2+}, and Zn^{2+}, promote catalysis in a large fraction of enzymes. Interestingly, it was shown that activity of enzymes is sensitive to not only a type of cation but also its concentration, e.g. DNA ligase III [50], RNase H [65], and Exonuclease VII [66]. For this reason, we analyzed the influence of increasing concentrations of Mg^{2+} ions and other divalent cations on the exonucleolytic activity of EXOG. The cleavage of ssDNA heterooligonucleotide was efficient at merely 0.1 mM concentration of Mg^{2+} ions (Supplementary Fig. S7 and lanes 2–6). Mn^{2+} ions stimulate the degradation of ssDNA even at the lowest 0.01 mM concentration tested (Supplementary Fig. S7 and lanes 15–18). However, we observed an inhibitory effect when 10 mM of Mn^{2+} was used in the reaction (Supplementary Fig. S7 and lane 18). Ca^{2+}, Fe^{2+}, Zn^{2+}, and Cu^{2+} ions do not or to a low degree support the activity of EXOG on ssDNA substrate.

EXOG cleaves single-stranded DNA flaps of various lengths

Since EXOG readily cleaves ssDNA of various lengths, we tested the cleavage of substrates designed to mimic flap-containing intermediates that may occur during DNA processing in mitochondria. We used nicked substrates with downstream 5′ flaps of various lengths (2, 7, 15, 30, or 60 nt), each fluorescently labeled at the 3′ terminus (Fig. 3A). While EXOG cleaved all substrates tested, the longest flaps were processed most efficiently (Fig. 3A and B). We also observed that the efficiency of cleavage decreased at the bottom of each flap following the removal of the first nucleotide from the DNA duplex. This is evident in the accumulation of a 19-nt long (indicated by the arrow in Fig. 3A) and shorter intermediate products. This observation strongly suggests that EXOG operates in fast and slow modes, with the mode of action dependent on the type of substrate destined for cleavage (ssDNA and dsDNA, respectively; Fig. 3C). Interestingly, blocking of the 5′ end of the 60-nt long flap with the biotin-streptavidin complex had little effect on the cleavage efficiency of EXOG (Supplementary Fig. S8), which contrasts with MGME1 nuclease whose DNA cleavage activity is inhibited when the 5′-end of the flap substrates is blocked [28]. Interestingly, to achieve similar efficiency of cleavage in time-course experiments, the molar ratio of a substrate to EXOG needed to be significantly higher in the nuclease assay with flap substrates (DNA:EXOG ratio of 4) compared with ssDNA (DNA:EXOG ratio of 400). We reason that the presence of DNA duplexes in the flap substrates influ-

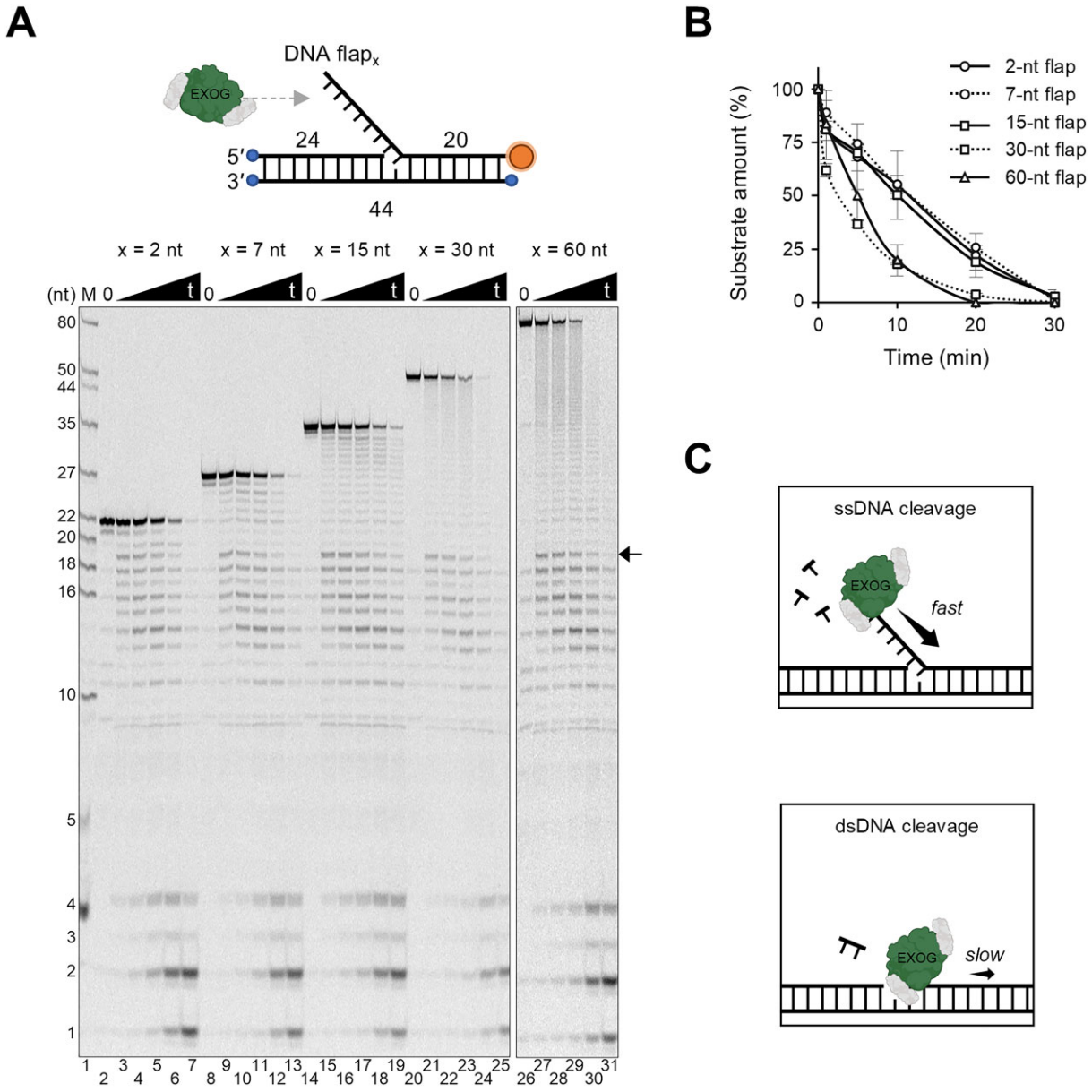

Figure 3. EXOG cleaves both short and long DNA flaps. (**A**) 800 nM of each substrate (S1–S5 and Supplementary Table S2) was incubated with 200 nM EXOG in the presence of 10 mM $MgCl_2$. Reactions were stopped at indicated time points (0, 1, 5, 10, 20, and 30 min) and analyzed using urea–PAGE. An arrow indicates bands corresponding with 19-nt long product. The scheme of the substrate is placed at the top of the panel. The 3′ end of the substrate strand is labeled with fluorescein; biotin is attached to the nonsubstrate ends of dsDNA; *M,* molecular-weight size marker. (**B**) Densitometric analysis of the substrate in panel (A). The graph represents the mean values with standard deviations (error bars) from two experiments. (**C**) Graphical model of the fast and slow cleavage mode of EXOG in the presence of ssDNA and dsDNA, respectively.

ences the cleavage efficiency of EXOG as the putative unspecific EXOG–dsDNA interactions could trap and prevent a portion of EXOG molecules from processing flaps or, more likely, EXOG might be trapped at the nick/gap site after flap cleavage.

Since all the tested 5′-flap substrates contained a nick, we then tested if varying length of a gap upstream from the flap may affect its processing by EXOG. The substrates examined contained 2, 15, or 60-nt 5′ flaps and 1, 2, 5, or 10-nt gaps (noncomplementary to flap sequences). Our results indicate that neither the flap nor the gap length significantly affected the efficiency of the cleavage by EXOG (Supplementary Fig. S9). Interestingly, after removing the flap in each gapped substrate, EXOG cleaves out 2 nucleotides (compared with 1 nucleotide in the case of nicked substrates in Fig. 3) from the downstream DNA duplex as an 18-nt long fragment is a dominant intermediate product that is apparent immediately after the reaction initiation (indicated by the arrows in Supplementary Fig. S9). This suggests that the mode of action of EXOG at the flap junction after a DNA flap removal depends on the proximity of the 3′ end of the upstream strand, which corresponds with the 3′ end of nascent DNA during extension process. Possibly the 3′ end at the nick site constitutes a steric hindrance for EXOG, making it significantly less efficient in delivering the target strand to the active site of the enzyme. In contrast, even a 1-nt gap might enhance the access of EXOG to its target at a 5′-single-stranded/duplex DNA junction after flap removal, leading EXOG to excise two nu-

cleotides from the downstream DNA duplex, which is in line with previously reported findings [43].

To corroborate the relevance of the Wing domain of EXOG to ssDNA processing, we further tested the deletion mutant EXOG-ΔC68 activity on substrates containing 15-nt long single-stranded flap of DNA, RNA, or RNA–DNA chimera. In agreement with the results from ssDNA/ssRNA cleavage assays (Fig. 1C–E), the EXOG-ΔC68 variant has impaired cleavage activity toward a DNA flap, while an RNA flap was processed with similar efficiency to EXOG (Supplementary Fig. S10 and lanes 1–10 and 31–40). In the case of a chimeric 2RNA-13DNA flap, the EXOG-ΔC68 variant also removed merely RNA, though with lower efficiency when compared with EXOG (Supplementary Fig. S10 and lanes 16–25). This result suggests that either 2RNA fragment is too short for efficient cleavage or the consecutive DNA fragment poses an obstacle to RNA processing by EXOG-ΔC68. Consistently, after RNA removal, DNA cleavage by EXOG-ΔC68 is inhibited. Finally, we tested EXOG-R109A mutant for flap cleavage and, similarly to EXOG-ΔC68, we did not observe the cleavage of the DNA flap (Supplementary Fig. S10 and lanes 11–15), while the RNA flap is cleaved as efficiently as by EXOG (Supplementary Fig. S10 and lanes 41–45). Interestingly, in the case of the chimeric flap, EXOG-R109A removed merely RNA, as EXOG-ΔC68; however, the efficiency of 2RNA fragment cleavage was comparable to EXOG (Supplementary Fig. S10 and lanes 26–30), suggesting that the presence of the Wing domain might increase the efficiency of short RNA cleavage. In all the reactions with EXOG-R109A, we can observe the accumulation of bands that correspond with the cleavage in the downstream double-stranded fragment of the substrates (marked with asterisks). We attribute these bands to nonspecific endo-cleavage by the EXOG-R109A mutant as no intermediate products characteristic for exonuclease activity can be detected. Together, these findings provide further confirmation that the Wing domain of EXOG as well as R109 in the Core domain are instrumental in conferring specificity toward ssDNA cleavage.

In contrast to ssDNA/ssRNA cleavage by EXOG (Supplementary Fig. S3), an RNA flap is cleaved more efficiently than a DNA flap (Supplementary Fig. S10, compare lanes 1–5 and 31–35), which implies that the presence of a double-stranded helix attached to a single-stranded substrate alters the efficiency of EXOG-mediated cleavage.

SSB-coated single-stranded DNA flaps are processed by EXOG

Single-stranded DNA flaps in mitochondria, much like any single-stranded DNA encountered during DNA processing, are bound and protected by mitochondrial single-stranded DNA-binding protein (mtSSB). Due to its high-affinity binding [67] and abundance in mitochondria [68], we investigated the influence of human mtSSB on flap cleavage by EXOG (Fig. 4A). It was previously shown that at physiological salt concentrations mtSSB tetramer forms a stable complex with a ssDNA molecule of at least ∼20 nucleotides in length and, depending on NaCl and Mg^{2+} concentrations, mtSSB tetramer displays two binding modes, SSB_{30} and SSB_{60} [69–71]. Therefore, we used substrates with 30- and 60-nt long flaps for this analysis. The given concentrations and ratios refer to tetramer of mtSSB and dimer of EXOG. The increasing ratio of mtSSB tetramer to substrate has an inhibitory effect on both flaps degradation by EXOG (Fig. 4B). The pattern of inhibition was similar for both substrates; at the SSB:DNA ratio of 1, the cleavage by EXOG was inhibited approximately by half for both 30- and 60-nt long flaps and saturation of the reaction was observed at SSB:DNA ratio = 5 (Fig. 4B and Supplementary Fig. S11). Since the strongest inhibitory effect of mtSSB on the flap cleavage by EXOG was observed for excessive amount of mtSSB in the reactions (4 μM mtSSB at the ratio of SSB:DNA = 5 in the presence of 200 nM EXOG, corresponding to SSB:EXOG ratio = 20), we analyzed if EXOG is able to outcompete mtSSB and cleave flap substrates. Both 30- and 60-nt long flaps were preincubated with mtSSB at the ratio of SSB:DNA = 5 in order to saturate DNA and afterward the increasing concentration of EXOG was added to the reactions. As the cleavage control, the same reactions were analyzed without mtSSB. The presence of mtSSB in the reactions clearly decelerated the processing of both flaps by EXOG (Fig. 4C, compare lanes 2–7 and 8–13 for 30-nt flap and lanes 14–19 and 20–25 for 60-nt flap). However, merely 0.2 ratio of EXOG:SSB was sufficient to observe substantial shortening of the flap substrates, indicating that EXOG is able to process mtSSB-coated flaps. Interestingly, we can observe an accumulation of bands (indicated by the arrows) of the same size regardless of the flap length (Fig. 4C, lanes 12–13 and 24–25 for 30- and 60-nt long flaps, respectively). We hypothesize that the appearance of these intermediate products, along with the substrate cleavage by EXOG at submolar concentration relative to mtSSB, indicate a more intricate interplay between EXOG, mtSSB, and ssDNA. These interactions may play a significant role in ssDNA flap removal rather than a straightforward displacement of mtSSB by EXOG.

DNA flaps removal by EXOG provides substrates for ligation

To investigate the relevance of EXOG in DNA flaps removal, we tested if and how efficiently the post-cleavage ligation occurs. First, we tested the ligation of flap-containing linear substrates in reactions including 5 nM EXOG and 200 nM substrate with either a short (2 nt) or long (15 nt) DNA flap, supplemented with 200 nM Lig III. The ligated product should be observed as a 44-nt long band (scheme of the reaction in Supplementary Fig. S12A). Substrates containing both DNA flaps were not efficiently ligated in the presence of EXOG and Lig III (Supplementary Fig. S12B, and lanes 4 and 8). The addition of Pol γ moderately increased ligation efficiency (Supplementary Fig. S12B, and lanes 5 and 9). This finding is in line with our observation that EXOG excises one nucleotide from the downstream DNA duplex after DNA flap removal (Fig. 3A) thus generating an unligatable 1-nt gap. The Pol γ activity might therefore fill in the gap or prevent EXOG from the gap formation.

Due to the high reactivity of EXOG toward 5′ ends of linear DNA, we blocked all the nonsubstrate DNA ends with biotin–streptavidin complexes. Additionally, after 10 min of incubation with EXOG, unlabeled competitor ssDNA was added to prevent excessive cleavage. Despite the fact that ∼50% of the substrate was processed by EXOG, we observed modest ligation efficiency (∼15% for both 2-nt and 15-nt DNA flaps) for linear substrates in the presence of EXOG, Pol γ, and Lig III (Supplementary Fig. S12C). To eliminate the presence of free DNA ends, we reconstituted the ligation reaction on a circular template primed with DNA oligonucleotides that contained

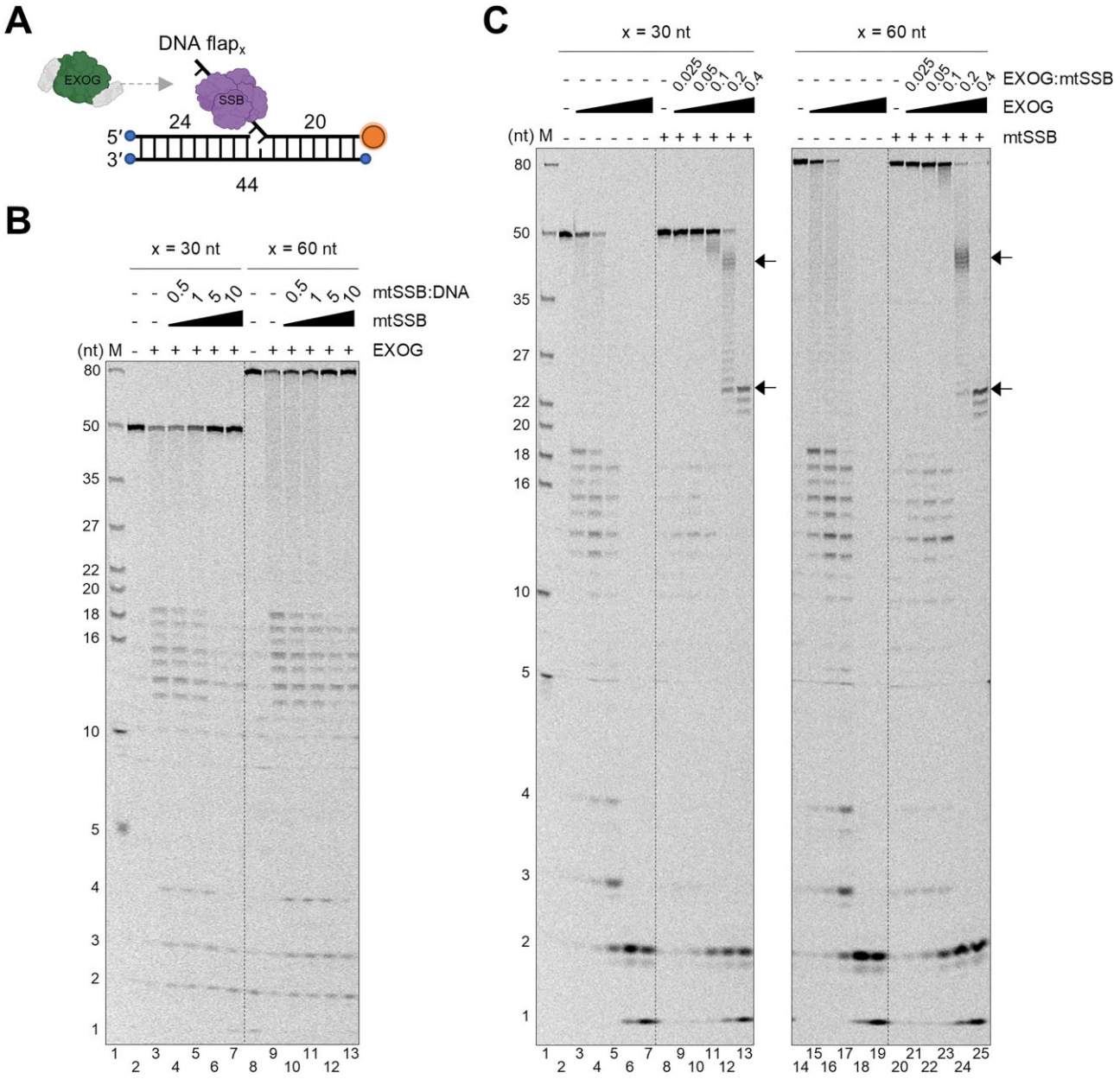

Figure 4. EXOG processes mtSSB-coated DNA flaps. (**A**) Scheme of the reactions in panels (**B**) and (**C**). DNA flap-containing substrates (30-nt flap S4 and 60-nt flap S5; Supplementary Table S2) were coated with human mtSSB before the addition of EXOG. The 3′ end of the substrate strand is labeled with fluorescein; biotin is attached to the nonsubstrate ends of dsDNA. The given concentrations and ratios refer to tetramer of mtSSB and dimer of EXOG. (**B**) 800 nM of each substrate was preincubated with mtSSB at indicated ratios (0.5, 1, 5, and 10 per SSB tetramer) for 10 min at RT in the presence of 10 mM $MgCl_2$. The reactions were started by the addition of 200 nM EXOG, stopped after further 10 min of incubation and analyzed using urea–PAGE. Densitometric analysis of the substrates is provided in Supplementary Fig. S11. (**C**) 800 nM of each substrate was preincubated with 4 μM mtSSB (SSB:DNA = 5) for 10 min at RT in the presence of 10 mM $MgCl_2$. The reactions were started by the addition of the increasing concentration of EXOG (100, 200, 400, 800, and 1600 nM). As a control, the same reactions were carried out without mtSSB. After 10 min of incubation, reactions were stopped and analyzed using urea–PAGE; *M*, molecular-weight size marker.

2- or 15-nt DNA flap. The reactions were initiated by Pol γ-mediated primer extension in the presence of mtSSB to convert single-stranded template into a double-stranded intermediate. Subsequently, EXOG and Lig III were added (Fig. 5A). DNA was labeled by Pol γ as a result of [α-^{32}P] dCTP incorporation during primer extension; therefore, unprocessed substrates were not detected. Since only upon ligation the newly synthesized strand becomes circular, all the reaction intermediates are detected as linear fragments. The migration of linear DNA is uniform and related to the length of DNA fragments, while mobility of circular DNA is slower in high voltage unidirectional electric fields. Thus, one can observe well-resolved linear fragments at the bottom of the gel and circular fragments at the top. In the reactions with Pol γ and mtSSB alone, we observed bands corresponding with a newly synthesized strand (Fig. 5B, and lanes 2 and 6). Subsequent addition of EXOG resulted in the cleavage of unligated intermediate in the absence of Lig III (Fig. 5B, and lanes 3 and 7). The addition of Lig III alone did not affect the reactions (Fig. 5B, and lanes 4 and 8). Only when both EXOG and Lig III were added to

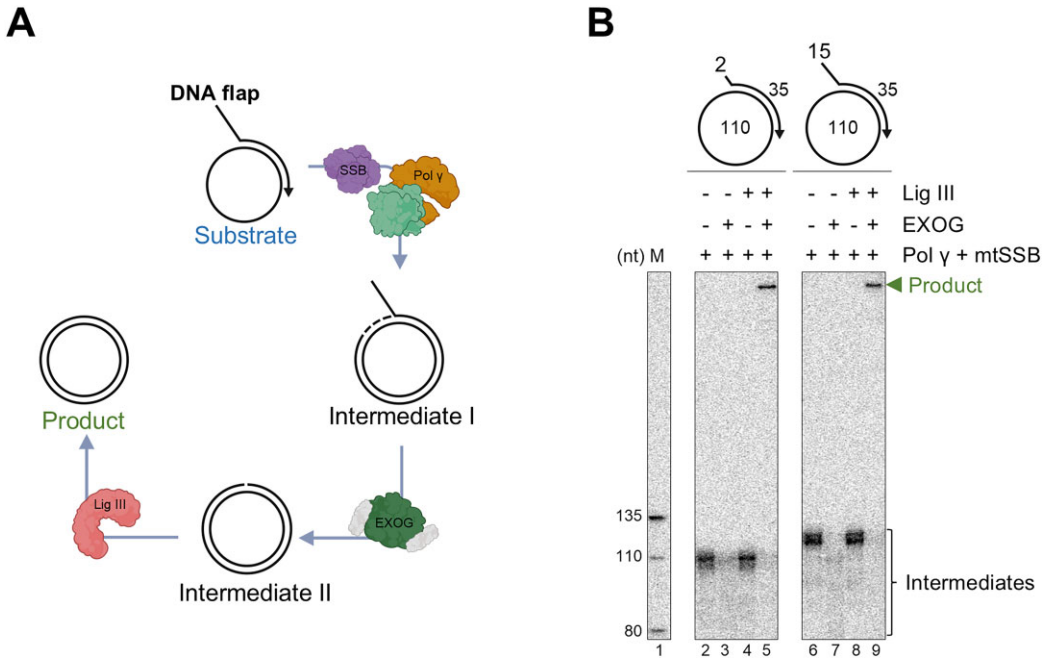

Figure 5. DNA flaps removal by EXOG supports ligation of circular substrates. (**A**) Scheme of the ligation reaction on a circular substrate containing DNA flap. The primer of the single-stranded substrate is extended by Pol γ in the presence of mtSSB (Intermediate I). EXOG removes DNA flap and a potential gap is filled by Pol γ (Intermediate II). Lig III seals a nick forming a closed double-stranded circular product. (**B**) The assay was performed as described in "Materials and methods" section. Briefly, substrate was preincubated with Pol γ and mtSSB for 20 min at 37°C, followed by the addition of EXOG and Lig III. After 1 h of incubation at 37°C, reactions were stopped and analyzed using urea–PAGE. [α-^{32}P] dCTP incorporated by Pol γ allowed detection of the intermediates (bracket) and final product (arrowhead). The substrate is not visible due to a lack of labeling. Schemes of the substrates (S21 and S22, and Supplementary Table S2) are placed at the top of the panel; *M*, molecular-weight size marker of linear DNA.

the reaction, we observed a band corresponding with a closed circular product (Fig. 5B, and lanes 5 and 9). Importantly, the intermediates were fully cleared from the reaction, which we attribute to either highly efficient ligation or the cleavage of the unligated intermediates by EXOG. Together, our results show that EXOG is able to remove DNA flaps and, in the presence of Pol γ, mtSSB and Lig III, supports subsequent ligation of tested substrates.

Discussion

It was previously shown that human mitochondrial nuclease EXOG cleaves ssDNA [40, 45], and the deletion of the C-terminal Wing domain inhibits its exonuclease activity toward ssDNA [40] as well as specificity for dsDNA repair intermediates [43]. Here, we analyzed the relevance of the Wing domain to the exonucleolytic activity of EXOG and we found that the deletion mutant EXOG-ΔC68 exhibits significantly reduced cleavage activity toward ssDNA but not ssRNA (Fig. 1C–E). We observed similar results for substrates containing DNA and RNA 5′ flaps (Supplementary Fig. S10). The lower activity stems from the impaired ssDNA binding and positioning in the active site of the EXOG deletion mutant (Fig. 1F), which we also explored in detail using MD simulations. Curiously, EXOG-ΔC68 cleaves ssRNA more efficiently than EXOG, regardless of salt concentration (Fig. 1D). The cleavage efficiency of a long RNA flap was similar for both EXOG variants, which could be explained by the different persistence length (flexibility) of the flaps attached to a double-stranded helix when compared with solely single-stranded molecules [72]. The observed specificity of substrate cleavage by the EXOG-ΔC68 variant is in agreement with the cleavage specificity of human EndoG, which was shown to be independent of salt concentration for RNA cleavage, while the increasing KCl concentration was inhibitory for the DNA cleavage efficiency [73]. The substrate-binding site of both EndoG and EXOG-ΔC68 is a solvent-exposed surface with backbone-mediated recognition, meaning that bases of a single-stranded substrate are oriented toward the solvent and the sugar rings directly interact with the protein (Supplementary Fig. S13). Protein–RNA interaction might occur via a hydroxyl group at position 2 of ribose, whereas this interaction is not available for protein–DNA complexes [74]. Therefore, the chemical and structural differences between RNA and DNA might explain the observed differences in interactions, which is additionally supported by our MD simulations results (Supplementary Fig. S4B). In contrast, the Wing domain of EXOG forms a positively charged V-shaped cleft with the Core domain [43] which sequesters the binding site from the solvent and locks its DNA substrate in the active site. Interestingly, our MD simulations also revealed a crucial role of R109 residue (located in the active region of the Core domain of EXOG) in ssDNA but not ssRNA positioning in the active site. Our biochemical analysis confirmed these findings (Supplementary Figs S4E and S10). This finding suggests that the presence of the unique Wing domain in EXOG structure together with the Core domain architecture form a specialized active region that allows binding and processing of ssDNA substrates.

Flaps are single-stranded 5′ overhangs on a duplex DNA, formed as a result of, e.g. strand displacement DNA synthesis. We demonstrate that EXOG cleaves DNA flaps independently of their length (Fig. 3) and the gap size within a ds-DNA (Supplementary Fig. S9). Moreover, 5′ ends of the long

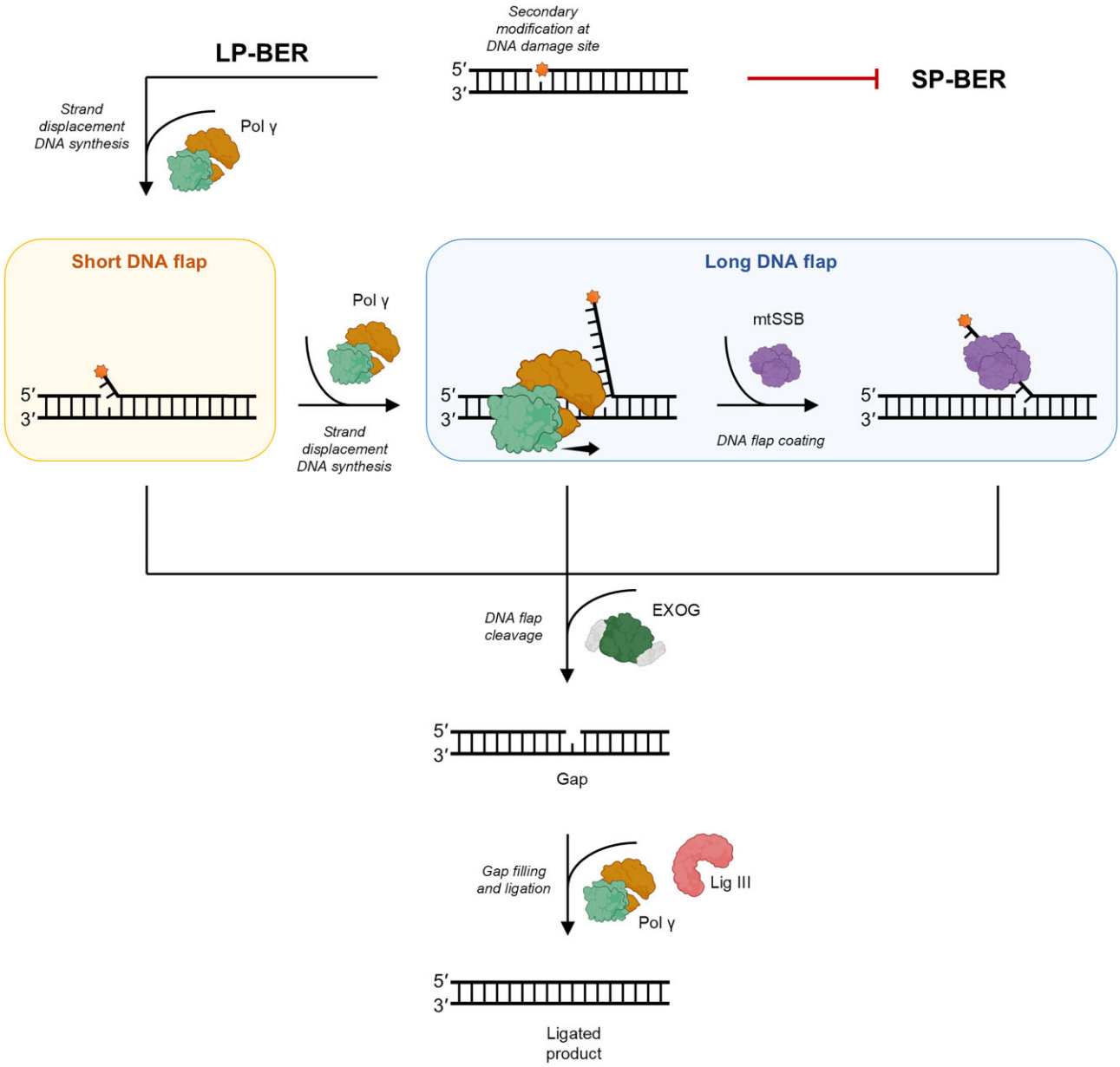

Figure 6. Schematic model for the role of EXOG in DNA flap cleavage during LP-BER in mitochondria. Secondary modifications of DNA backbone at damage sites result in inhibition of short-patch BER (SP-BER), which triggers an alternative long-patch BER (LP-BER) pathway. Strand displacement DNA synthesis activity of Pol γ at the modified damage site generates either short (1–2 nt) or long (>2 nt) single-stranded 5′ DNA flaps. Long single-stranded DNA overhangs are coated by mtSSB. EXOG cleaves short and long DNA flaps as well as mtSSB-coated flaps. As a result, gapped DNA is formed, which is filled by Pol γ and sealed by Lig III.

flaps blocked with biotin–streptavidin complexes are removed with similar efficiency to the 5′ end with no modification (Supplementary Fig. S8), in agreement with our recently published data [44]. This shows that EXOG is not sensitive to 5′-end modifications of a flap and suggests the ability to remove flaps with modified or blocked 5′ ends that occurs during canonical LP-BER, as was reported for FEN1 [75], while the activity of MGME1 is inhibited when the 5′-end of the flap is blocked [28]. In addition to our recently reported hydrolysis activity of EXOG on a variety of abasic sites at a 5′ end of a gapped dsDNA, including 5′-deoxyribose phosphate (dRP) and its oxidized adduct deoxyribonolactone (dL) [44], we propose that EXOG might be involved in both canonical LP-BER that requires the removal of displaced ssDNA and noncanonical LP-BER. In the noncanonical pathway, EXOG would excise a lesion along with a downstream dinucleotide, thus generating a gap that is filled by polymerase.

To date, no structural data on EXOG in complex with ssDNA or ssRNA are available. In our group, we attempted to grow crystals of such complexes but so far failed to obtain high-resolution diffraction data. Therefore, we conducted a comparative analysis using existing structures of human EXOG–dsDNA [43] and *Caenorhabditis elegans* EndoG homolog, CPS-6, in complex with ssDNA [76]. The substrate strand of dsDNA accommodates in the binding site of EXOG in a similar manner to the ssDNA at the binding site of EndoG (Supplementary Fig. S13C; the complementary strand and the Wing domain of EXOG is hidden for clarity), which was not

surprising as the Core dimers of both proteins are nearly identical (RMSD = 0.776 Å). If the substrate strand of dsDNA is bound to the active site of EXOG in a similar manner as ssDNA in the active site of EndoG, one can assume that the ssDNA substrate is also similarly located in the active site of EXOG. However, we observe different efficiency and cleavage specificity for ssDNA and dsDNA: ssDNA is cleaved fast with mononucleotides being released, while the removal of a substrate strand from dsDNA is slower and predominantly in the form of dinucleotides (Fig. 3). Additionally, we compared the substrate DNA strand position in the EXOG–dsDNA crystal structure with ssDNA position in our model structure of EXOG–ssDNA complex (Supplementary Fig. S14). According to our MD simulations, the occupancy of ssDNA in the active region of EXOG structure differs from the substrate strand of dsDNA. Therefore, the observed bimodal activity of EXOG might be related to a different occupancy of the active site by both substrates, different conformation of the Wing domain or differences in product release. It is noteworthy that ssDNA cleavage is sequence non-specific, although the efficiency is moderately dependent on the type of a nucleotide in a sequence (Fig. 2). A high-resolution structure of EXOG with a single-stranded substrate is indispensable to explain its unusual activity switch depending on the strandedness of a substrate.

Finally, we demonstrated that EXOG cleaves DNA flaps in the presence of other mitochondrial proteins. mtSSB-coated flaps (30- and 60-nt long) are readily processed by EXOG with certain bands accumulated, irrespective of the flap length (Fig. 4C). Given that EXOG can also function as an endonuclease, it might recognize ssDNA in the mtSSB–flap complex and cleave it in the endo-mode of action, thus causing destabilization and dissociation of mtSSB from ssDNA. Alternatively, EXOG might push mtSSB in the 5′ to 3′ direction toward a downstream duplex, resulting in the melting of the base pairs. This mechanism was shown in other systems, such as the filament growth of RecA and the SSB-facilitated melting of the hairpin structure [77] as well as the stable unwinding of a duplex DNA by human RPA (nuclear SSB) due to the Pif1 helicase-mediated translocation [78]. The nature of this reaction remains to be elucidated. In the final analysis, we reconstituted a multistep reaction combining DNA synthesis, DNA flap removal, and nick ligation in the presence of Pol γ, mtSSB, EXOG, and Lig III. Circular substrates containing short (2 nt) and long (15 nt) flaps were efficiently processed into ligated double-stranded products (Fig. 5), which requires the conjoint action of all the proteins. In the absence of Lig III, when the final ligated product cannot be obtained, EXOG cleaves the intermediate product generated by Pol γ, thus protecting from the accumulation of DNA breaks. When Lig III is present, EXOG removes the flaps and does not interfere with the ligation reaction by excessive cleavage. We carried out analogous reactions using linear substrates; however, the efficiency of ligation was low (Supplementary Fig. S12). This might be explained by the trapping of EXOG on the 5′ ends of the duplex DNA and/or the downstream strand displacement by Pol γ. Therefore, the advantage of circular over linear substrate is not only the absence of nonsubstrate 5′ ends but also negligibility of Pol γ-mediated strand displacement.

To conclude, we propose that EXOG should be considered as one of the mitochondrial DNA flap nucleases that is involved in LP-BER in mitochondria (Fig. 6). Even though the role of EXOG in LP-BER was previously reported in mitochondrial extracts [11, 26], its enzymatic capabilities have not been explored in detail. We show that EXOG processes both short and long DNA flaps, and the presence of the Wing domain in the structure of EXOG facilitates the binding, proper positioning, and cleavage of ssDNA at physiological salt conditions. Most importantly, the removal of DNA flaps by EXOG generates ligatable intermediates. When combined with Pol γ, mtSSB, and Lig III, substrates with 5′ DNA overhangs are transformed into fully processed dsDNA, underscoring the critical role of EXOG in human mitochondrial DNA integrity.

Acknowledgements

We thank Grzegorz Grabe (University of Gdansk) for discussions and critical reading of the manuscript. Molecular graphics and analyses were performed with UCSF ChimeraX [79], developed by the Resource for Biocomputing, Visualization, and Informatics at the University of California, San Francisco, with support from the National Institutes of Health (R01-GM129325) and the Office of Cyber Infrastructure and Computational Biology, National Institute of Allergy and Infectious Diseases. Graphical abstract and figures elements (proteins and ssDNA/ssRNA icons) were created in BioRender.com: https://BioRender.com/p80x724 and https://BioRender.com/y05h957. ImageJ was used for band quantification [51]. MD simulations were carried out using the computers of CI TASK (Gdańsk).

Author contributions: A.K. and M.R.S: conceptualization; A.K., A.B.D., M.W., K.A.H., J.C., and M.R.S.: resources; A.K., A.B.D., M.W., K.A.H., J.C., and M.R.S.: data curation; A.K. and M.R.S.: formal analysis; A.K. and M.R.S.: validation; A.K., A.B.D., M.W., K.A.H., J.C. and M.R.S.: investigation; A.K., K.A.H., J.C., and M.R.S.: visualization; A.K., A.B.D., M.W., K.A.H., J.C., and M.R.S.: methodology; A.K. and M.R.S.: writing—original draft; A.K., A.B.D., M.W., K.A.H., J.C., and M.R.S.: writing—review and editing; M.R.S.: supervision; M.R.S.: funding acquisition; M.R.S.: project administration.

Supplementary data

Supplementary data is available at NAR online.

Conflict of interest

None declared.

Funding

This work was supported by the First TEAM program, co-financed by the Foundation for Polish Science and the European Union under the European Regional Development Fund [POIR.04.04.00-00-3E44/17-00 to M.R.S.]; the European Research Council (ERC) under the European Union's Horizon 2020 research and innovation program [852662 to M.R.S.]; and the EMBO Installation Grant [4129 to M.R.S.]. Funding to pay the Open Access publication charges for this article was provided by the University of Gdansk, Poland.

Data availability

The molecular dynamics data underlying this article are available in Figshare at https://doi.org/10.6084/m9.figshare.28270808.

References

1. Roger AJ, Muñoz-Gómez SA, Kamikawa R. The origin and diversification of mitochondria. *Curr Biol* 2017;**27**:R1177–92. https://doi.org/10.1016/j.cub.2017.09.015
2. Piovesan A, Pelleri MC, Antonaros F *et al.* On the length, weight and GC content of the human genome. *BMC Res Notes* 2019;**12**:106. https://doi.org/10.1186/s13104-019-4137-z
3. Tuppen HA, Blakely EL, Turnbull DM *et al.* Mitochondrial DNA mutations and human disease. *Biochim Biophys Acta* 2010;**1797**:113–28. https://doi.org/10.1016/j.bbabio.2009.09.005
4. Kazak L, Reyes A, Holt IJ. Minimizing the damage: repair pathways keep mitochondrial DNA intact. *Nat Rev Mol Cell Biol* 2012;**13**:659–71. https://doi.org/10.1038/nrm3439
5. Fu Y, Tigano M, Sfeir A. Safeguarding mitochondrial genomes in higher eukaryotes. *Nat Struct Mol Biol* 2020;**27**:687–95. https://doi.org/10.1038/s41594-020-0474-9
6. Rong Z, Tu P, Xu P *et al.* The mitochondrial response to DNA damage. *Front Cell Dev Biol* 2021;**9**:669379. https://doi.org/10.3389/fcell.2021.669379
7. Krokan HE, Bjoras M. Base excision repair. *Cold Spring Harb Perspect Biol* 2013;**5**:a012583. https://doi.org/10.1101/cshperspect.a012583
8. McKinnon PJ, Caldecott KW. DNA strand break repair and human genetic disease. *Annu Rev Genom Hum Genet* 2007;**8**:37–55. https://doi.org/10.1146/annurev.genom.7.080505.115648
9. Liu P, Qian L, Sung J-S *et al.* Removal of oxidative DNA damage via FEN1-dependent long-patch base excision repair in human cell mitochondria. *Mol Cell Biol* 2008;**28**:4975–87. https://doi.org/10.1128/MCB.00457-08
10. Sattler U, Frit P, Salles B *et al.* Long-patch DNA repair synthesis during base excision repair in mammalian cells. *EMBO Rep* 2003;**4**:363–7. https://doi.org/10.1038/sj.embor.embor796
11. Szczesny B, Tann AW, Longley MJ *et al.* Long patch base excision repair in mammalian mitochondrial genomes. *J Biol Chem* 2008;**283**:26349–56. https://doi.org/10.1074/jbc.M803491200
12. Akbari M, Visnes T, Krokan HE *et al.* Mitochondrial base excision repair of uracil and AP sites takes place by single-nucleotide insertion and long-patch DNA synthesis. *DNA Repair* 2008;**7**:605–16. https://doi.org/10.1016/j.dnarep.2008.01.002
13. Robertson AB, Klungland A, Rognes T *et al.* DNA repair in mammalian cells: base excision repair: the long and short of it. *Cell Mol Life Sci* 2009;**66**:981–93. https://doi.org/10.1007/s00018-009-8736-z
14. Plaza GAI, Lemishko KM, Crespo R *et al.* Mechanism of strand displacement DNA synthesis by the coordinated activities of human mitochondrial DNA polymerase and SSB. *Nucleic Acids Res* 2023;**51**:1750–65. https://doi.org/10.1093/nar/gkad037
15. Shereda RD, Kozlov AG, Lohman TM *et al.* SSB as an organizer/mobilizer of genome maintenance complexes. *Crit Rev Biochem Mol Biol* 2008;**43**:289–318. https://doi.org/10.1080/10409230802341296
16. Ciesielski GL, Bermek O, Rosado-Ruiz FA *et al.* Mitochondrial single-stranded DNA-binding proteins stimulate the activity of DNA polymerase γ by organization of the template DNA. *J Biol Chem* 2015;**290**:28697–707. https://doi.org/10.1074/jbc.M115.673707
17. Yang C, Curth U, Urbanke C *et al.* Crystal structure of human mitochondrial single-stranded DNA binding protein at 2.4 A resolution. *Nat Struct Mol Biol* 1997;**4**:153–7. https://doi.org/10.1038/nsb0297-153
18. Raghunathan S, Ricard CS, Lohman TM *et al.* Crystal structure of the homo-tetrameric DNA binding domain of *Escherichia coli* single-stranded DNA-binding protein determined by multiwavelength X-ray diffraction on the selenomethionyl protein at 2.9-Å resolution. *Proc Natl Acad Sci USA* 1997;**94**:6652–7. https://doi.org/10.1073/pnas.94.13.6652
19. Ruhanen H, Borrie S, Szabadkai G *et al.* Mitochondrial single-stranded DNA binding protein is required for maintenance of mitochondrial DNA and 7S DNA but is not required for mitochondrial nucleoid organisation. *Biochim Biophys Acta Mol Cell Res* 2010;**1803**:931–9. https://doi.org/10.1016/j.bbamcr.2010.04.008
20. Korhonen JA, Gaspari M, Falkenberg M. TWINKLE has 5′ → 3′ DNA helicase activity and is specifically stimulated by mitochondrial single-stranded DNA-binding protein. *J Biol Chem* 2003;**278**:48627–32. https://doi.org/10.1074/jbc.M306981200
21. Farr CL, Matsushima Y, Lagina AT 3rd *et al.* Physiological and biochemical defects in functional interactions of mitochondrial DNA polymerase and DNA-binding mutants of single-stranded DNA-binding protein. *J Biol Chem* 2004;**279**:17047–53. https://doi.org/10.1074/jbc.M400283200
22. Korhonen JA, Pham XH, Pellegrini M *et al.* Reconstitution of a minimal mtDNA replisome in vitro. *EMBO J* 2004;**23**:2423–9. https://doi.org/10.1038/sj.emboj.7600257
23. Jiang M, Xie X, Zhu X *et al.* The mitochondrial single-stranded DNA binding protein is essential for initiation of mtDNA replication. *Sci Adv* 2021;**7**:eabf8631. https://doi.org/10.1126/sciadv.abf8631
24. Szczesny RJ, Hejnowicz MS, Steczkiewicz K *et al.* Identification of a novel human mitochondrial endo-/exonuclease Ddk1/c20orf72 necessary for maintenance of proper 7S DNA levels. *Nucleic Acids Res* 2013;**41**:3144–61. https://doi.org/10.1093/nar/gkt029
25. Zheng L, Zhou M, Guo Z *et al.* Human DNA2 is a mitochondrial nuclease/helicase for efficient processing of DNA replication and repair intermediates. *Mol Cell* 2008;**32**:325–36. https://doi.org/10.1016/j.molcel.2008.09.024
26. Tann AW, Boldogh I, Meiss G *et al.* Apoptosis induced by persistent single-strand breaks in mitochondrial genome: critical role of EXOG (5′-EXO/endonuclease) in their repair. *J Biol Chem* 2011;**286**:31975–83. https://doi.org/10.1074/jbc.M110.215715
27. Kornblum C, Nicholls TJ, Haack TB *et al.* Loss-of-function mutations in MGME1 impair mtDNA replication and cause multisystemic mitochondrial disease. *Nat Genet* 2013;**45**:214–9. https://doi.org/10.1038/ng.2501
28. Uhler JP, Thörn C, Nicholls TJ *et al.* MGME1 processes flaps into ligatable nicks in concert with DNA polymerase γ during mtDNA replication. *Nucleic Acids Res* 2016;**44**:5861–71. https://doi.org/10.1093/nar/gkw468
29. Matic S, Jiang M, Nicholls TJ *et al.* Mice lacking the mitochondrial exonuclease MGME1 accumulate mtDNA deletions without developing progeria. *Nat Commun* 2018;**9**:1202. https://doi.org/10.1038/s41467-018-03552-x
30. Budd ME, Campbell JL. A yeast replicative helicase, Dna2 helicase, interacts with yeast FEN-1 nuclease in carrying out its essential function. *Mol Cell Biol* 1997;**17**:2136–42. https://doi.org/10.1128/MCB.17.4.2136
31. Bae S-H, Seo Y-S. Characterization of the enzymatic properties of the yeast dna2 helicase/endonuclease suggests a new model for Okazaki fragment processing. *J Biol Chem* 2000;**275**:38022–31. https://doi.org/10.1074/jbc.M006513200
32. Bae S-H, Bae K-H, Kim J *et al.* RPA governs endonuclease switching during processing of Okazaki fragments in eukaryotes. *Nature* 2001;**412**:456–61. https://doi.org/10.1038/35086609
33. Ayyagari R, Gomes XV, Gordenin DA *et al.* Okazaki fragment maturation in yeast: I. Distribution of functions between FEN1 and DNA2. *J Biol Chem* 2003;**278**:1618–25. https://doi.org/10.1074/jbc.M209801200
34. Kao H-I, Veeraraghavan J, Polaczek P *et al.* On the roles of *Saccharomyces cerevisiae* Dna2p and flap endonuclease 1 in

Okazaki fragment processing. *J Biol Chem* 2004;**279**:15014–24. https://doi.org/10.1074/jbc.M313216200
35. Kalifa L, Beutner G, Phadnis N *et al.* Evidence for a role of FEN1 in maintaining mitochondrial DNA integrity. *DNA Repair* 2009;**8**:1242–9. https://doi.org/10.1016/j.dnarep.2009.07.008
36. Kazak L, Reyes A, He J *et al.* A cryptic targeting signal creates a mitochondrial FEN1 isoform with tailed R-loop binding properties. *PLoS One* 2013;**8**:e62340. https://doi.org/10.1371/journal.pone.0062340
37. Karlowicz A, Dubiel AB, Czerwinska J *et al.* *In vitro* reconstitution reveals a key role of human mitochondrial EXOG in RNA primer processing. *Nucleic Acids Res* 2022;**50**:7991–8007. https://doi.org/10.1093/nar/gkac581
38. Duxin JP, Dao B, Martinsson P *et al.* Human Dna2 is a nuclear and mitochondrial DNA maintenance protein. *Mol Cell Biol* 2009;**29**:4274–82. https://doi.org/10.1128/MCB.01834-08
39. Stewart JA, Campbell JL, Bambara RA. Dna2 is a structure-specific nuclease, with affinity for 5′-flap intermediates. *Nucleic Acids Res* 2010;**38**:920–30. https://doi.org/10.1093/nar/gkp1055
40. Cymerman IA, Chung I, Beckmann BM *et al.* EXOG, a novel paralog of Endonuclease G in higher eukaryotes. *Nucleic Acids Res* 2008;**36**:1369–79. https://doi.org/10.1093/nar/gkm1169
41. Szczesny B, Olah G, Walker DK *et al.* Deficiency in repair of the mitochondrial genome sensitizes proliferating myoblasts to oxidative damage. *PLoS One* 2013;**8**:e75201. https://doi.org/10.1371/journal.pone.0075201
42. Xiao J, Dong X, Peng K *et al.* PGC-1α mediated-EXOG, a specific repair enzyme for mitochondrial DNA, plays an essential role in the rotenone-induced neurotoxicity of PC12 cells. *J Mol Neurosci* 2021;**71**:2336–52. https://doi.org/10.1007/s12031-020-01775-6
43. Szymanski MR, Yu W, Gmyrek AM *et al.* A domain in human EXOG converts apoptotic endonuclease to DNA-repair exonuclease. *Nat Commun* 2017;**8**:14959. https://doi.org/10.1038/ncomms14959
44. Szymanski MR, Karlowicz A, Herrmann GK *et al.* Human EXOG possesses strong AP hydrolysis activity: implication on mitochondrial DNA base excision repair. *J Am Chem Soc* 2022;**144**:23543–50. https://doi.org/10.1021/jacs.2c10558
45. Wu C-C, Lin JLJ, Yang-Yen H-F *et al.* A unique exonuclease ExoG cleaves between RNA and DNA in mitochondrial DNA replication. *Nucleic Acids Res* 2019;**47**:5405–19. https://doi.org/10.1093/nar/gkz241
46. Ohsato T, Ishihara N, Muta T *et al.* Mammalian mitochondrial endonuclease G. Digestion of R-loops and localization in intermembrane space. *Eur J Biochem* 2002;**269**:5765–70. https://doi.org/10.1046/j.1432-1033.2002.03238.x
47. Wu CC, Lin JLJ, Yuan HS. Structures, mechanisms, and functions of his-me finger nucleases. *Trends Biochem Sci* 2020;**45**:935–46. https://doi.org/10.1016/j.tibs.2020.07.002
48. Loll B, Gebhardt M, Wahle E *et al.* Crystal structure of the EndoG/EndoGI complex: mechanism of EndoG inhibition. *Nucleic Acids Res* 2009;**37**:7312–20. https://doi.org/10.1093/nar/gkp770
49. Szymanski MR, Kuznetsov VB, Shumate C *et al.* Structural basis for processivity and antiviral drug toxicity in human mitochondrial DNA replicase. *EMBO J* 2015;**34**:1959–70. https://doi.org/10.15252/embj.201591520
50. McNally JR, O'Brien PJ. Kinetic analyses of single-stranded break repair by human DNA ligase III isoforms reveal biochemical differences from DNA ligase I. *J Biol Chem* 2017;**292**:15870–9. https://doi.org/10.1074/jbc.M117.804625
51. Schneider CA, Rasband WS, Eliceiri KW. NIH image to ImageJ: 25 years of image analysis. *Nat Methods* 2012;**9**:671–5. https://doi.org/10.1038/nmeth.2089
52. Zillner K, Jerabek-Willemsen M, Duhr S *et al.* Microscale thermophoresis as a sensitive method to quantify protein: nucleic acid interactions in solution. *Methods Mol Biol* 2012;**815**:241–52. https://doi.org/10.1007/978-1-61779-424-7_18
53. Jerabek-Willemsen M, André T, Wanner R *et al.* MicroScale thermophoresis: interaction analysis and beyond. *J Mol Struct* 2014;**1077**:101–13. https://doi.org/10.1016/j.molstruc.2014.03.009
54. Abraham MJ, Murtola T, Schulz R *et al.* GROMACS: high performance molecular simulations through multi-level parallelism from laptops to supercomputers. *SoftwareX* 2015;**1-2**:19–25. https://doi.org/10.1016/j.softx.2015.06.001
55. Ivani I, Dans PD, Noy A *et al.* Parmbsc1: a refined force field for DNA simulations. *Nat Methods* 2016;**13**:55–8. https://doi.org/10.1038/nmeth.3658
56. Bussi G, Donadio D, Parrinello M. Canonical sampling through velocity rescaling. *J Chem Phys* 2007;**126**:014101. https://doi.org/10.1063/1.2408420
57. Parrinello M, Rahman A. Polymorphic transitions in single crystals: a new molecular dynamics method. *J Appl Phys* 1981;**52**:7182–90. https://doi.org/10.1063/1.328693
58. York DM, Darden TA, Pedersen LG. The effect of long-range electrostatic interactions in simulations of macromolecular crystals: a comparison of the Ewald and truncated list methods. *J Chem Phys* 1993;**99**:8345–8. https://doi.org/10.1063/1.465608
59. Hess B. P-LINCS: A parallel linear constraint solver for molecular simulation. *J Chem Theory Comput* 2008;**4**:116–22. https://doi.org/10.1021/ct700200b
60. Miyamoto S, Kollman PA. Settle: an analytical version of the SHAKE and RATTLE algorithm for rigid water models. *J Comput Chem* 1992;**13**:952–62. https://doi.org/10.1002/jcc.540130805
61. Killilea DW, Killilea AN. Mineral requirements for mitochondrial function: a connection to redox balance and cellular differentiation. *Free Radical Biol Med* 2022;**182**:182–91. https://doi.org/10.1016/j.freeradbiomed.2022.02.022
62. Urrutia KM, Xu W, Zhao L. The 5′-phosphate enhances the DNA-binding and exonuclease activities of human mitochondrial genome maintenance exonuclease 1 (MGME1). *J Biol Chem* 2022;**298**:102306. https://doi.org/10.1016/j.jbc.2022.102306
63. Hatters DM, Wilson L, Atcliffe BW *et al.* Sedimentation analysis of novel DNA structures formed by homo-oligonucleotides. *Biophys J* 2001;**81**:371–81. https://doi.org/10.1016/S0006-3495(01)75706-2
64. Richards EG, Flessel CP, Fresco JR. Polynucleotides. VI. Molecular properties and conformation of polyribouridylic acid. *Biopolymers* 1963;**1**:431–46. https://doi.org/10.1002/bip.360010504
65. Ho MH, De Vivo M, Dal Peraro M *et al.* Understanding the effect of magnesium ion concentration on the catalytic activity of ribonuclease H through computation: does a third metal binding site modulate endonuclease catalysis? *J Am Chem Soc* 2010;**132**:13702–12. https://doi.org/10.1021/ja102933y
66. Larrea AA, Pedroso IM, Malhotra A *et al.* Identification of two conserved aspartic acid residues required for DNA digestion by a novel thermophilic exonuclease VII in Thermotoga maritima. *Nucleic Acids Res* 2008;**36**:5992–6003. https://doi.org/10.1093/nar/gkn588
67. Chase JW, Williams KR. Single-stranded DNA binding proteins required for DNA replication. *Annu Rev Biochem* 1986;**55**:103–36. https://doi.org/10.1146/annurev.bi.55.070186.000535
68. Takamatsu C, Umeda S, Ohsato T *et al.* Regulation of mitochondrial D-loops by transcription factor A and single-stranded DNA-binding protein. *EMBO Rep* 2002;**3**:451–6. https://doi.org/10.1093/embo-reports/kvf099
69. Qian Y, Johnson KA. The human mitochondrial single-stranded DNA-binding protein displays distinct kinetics and thermodynamics of DNA binding and exchange. *J Biol Chem* 2017;**292**:13068–84. https://doi.org/10.1074/jbc.M117.791392
70. Morin JA, Cerrón F, Jarillo J *et al.* DNA synthesis determines the binding mode of the human mitochondrial single-stranded DNA-binding protein. *Nucleic Acids Res* 2017;**45**:7237–48. https://doi.org/10.1093/nar/gkx395

71. Kaur P, Longley MJ, Pan H *et al.* Single-molecule DREEM imaging reveals DNA wrapping around human mitochondrial single-stranded DNA binding protein. *Nucleic Acids Res* 2018;**46**:11287–302. https://doi.org/10.1093/nar/gky875
72. Chen H, Meisburger SP, Pabit SA *et al.* Ionic strength-dependent persistence lengths of single-stranded RNA and DNA. *Proc Natl Acad Sci USA* 2012;**109**:799–804. https://doi.org/10.1073/pnas.1119057109
73. Kalinowska M, Garncarz W, Pietrowska M *et al.* Regulation of the human apoptotic DNase/RNase endonuclease G: involvement of Hsp70 and ATP. *Apoptosis* 2005;**10**:821–30. https://doi.org/10.1007/s10495-005-0410-9
74. Hoffman MM, Khrapov MA, Cox JC *et al.* AANT: the amino acid-nucleotide interaction database. *Nucleic Acids Res* 2004;**32**:174D–181. https://doi.org/10.1093/nar/gkh128
75. Liu Y, Beard WA, Shock DD *et al.* DNA polymerase beta and flap endonuclease 1 enzymatic specificities sustain DNA synthesis for long patch base excision repair. *J Biol Chem* 2005;**280**:3665–74. https://doi.org/10.1074/jbc.M412922200
76. Lin JL, Wu CC, Yang WZ *et al.* Crystal structure of endonuclease G in complex with DNA reveals how it nonspecifically degrades DNA as a homodimer. *Nucleic Acids Res* 2016;**44**:10480–90.
77. Roy R, Kozlov AG, Lohman TM *et al.* SSB protein diffusion on single-stranded DNA stimulates RecA filament formation. *Nature* 2009;**461**:1092–7. https://doi.org/10.1038/nature08442
78. Mersch KN, Sokoloski JE, Nguyen B *et al.* "Helicase" activity promoted through dynamic interactions between a ssDNA translocase and a diffusing SSB protein. *Proc Natl Acad Sci USA* 2023;**120**:e2216777120. https://doi.org/10.1073/pnas.2216777120
79. Pettersen EF, Goddard TD, Huang CC *et al.* UCSF ChimeraX: structure visualization for researchers, educators, and developers. *Protein Sci* 2021;**30**:70–82. https://doi.org/10.1002/pro.3943

Received: February 27, 2024. **Revised:** January 27, 2025. **Editorial Decision:** January 29, 2025. **Accepted:** February 4, 2025